

RETRACTED

[View retraction](#)**Amendment history:**

- Retraction (January 2026)

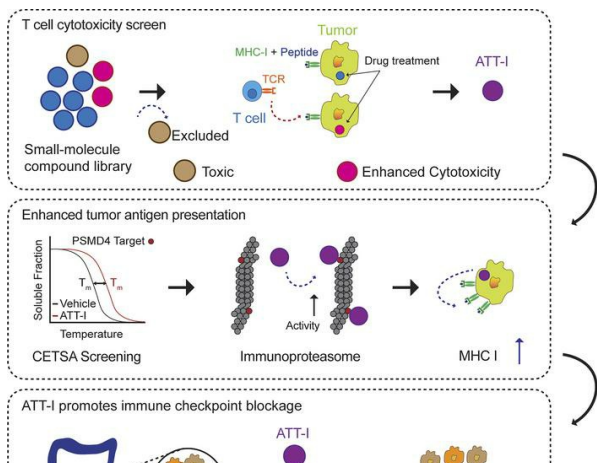
Atractylenolide I enhances responsiveness to immune checkpoint blockade therapy by activating tumor antigen presentation

Hanchen Xu, Kevin Van der Jeught, Zhuolong Zhou, Lu Zhang, Tao Yu, Yifan Sun, Yujing Li, Changlin Wan, Ka Man So, Degang Liu, Michael Frieden, Yuanzhang Fang, Amber L. Mosley, Xiaoming He, Xinna Zhang, George E. Sandusky, Yunlong Liu, Samy O. Meroueh, Chi Zhang, Aruna B. Wijeratne, Cheng Huang, Guang Ji, Xiongbin Lu

J Clin Invest. 2021;131(10):e146832. <https://doi.org/10.1172/JCI146832>.

Research Article **Immunology** **Oncology**

Graphical abstract



Find the latest version:

<https://jci.me/146832/pdf>



Atractylenolide I enhances responsiveness to immune checkpoint blockade therapy by activating tumor antigen presentation

Hanchen Xu,^{1,2} Kevin Van der Jeught,² Zhuolong Zhou,² Lu Zhang,^{1,2} Tao Yu,² Yifan Sun,² Yujing Li,² Changlin Wan,³ Ka Man So,³ Degang Liu,⁴ Michael Frieden,² Yuanzhang Fang,² Amber L. Mosley,^{4,5} Xiaoming He,^{6,7} Xinna Zhang,^{2,8} George E. Sandusky,⁹ Yunlong Liu,^{2,3,8} Samy O. Meroueh,⁴ Chi Zhang,^{2,3,8} Aruna B. Wijeratne,^{4,5} Cheng Huang,¹⁰ Guang Ji,¹ and Xiongbin Lu^{2,3,8}

¹Institute of Digestive Diseases, Longhua Hospital, Shanghai University of Traditional Chinese Medicine, Shanghai, China. ²Department of Medical and Molecular Genetics, ³Center for Computational Biology and Bioinformatics, ⁴Department of Biochemistry and Molecular Biology, and ⁵Proteomics Core Facility, Indiana University School of Medicine, Indianapolis, Indiana, USA. ⁶Fischell Department of Bioengineering, University of Maryland, College Park, Maryland, USA. ⁷Marlene and Stewart Greenebaum Comprehensive Cancer Center, University of Maryland, Baltimore, Maryland, USA. ⁸Melvin and Bren Simon Cancer Center and ⁹Department of Pathology and Laboratory Medicine, Indiana University School of Medicine, Indianapolis, Indiana, USA. ¹⁰Drug Discovery Laboratory, School of Pharmacy, Shanghai University of Traditional Chinese Medicine, Shanghai, China.

One of the primary mechanisms of tumor cell immune evasion is the loss of antigenicity, which arises due to lack of immunogenic tumor antigens as well as dysregulation of the antigen processing machinery. In a screen for small-molecule compounds from herbal medicine that potentiate T cell-mediated cytotoxicity, we identified atractylenolide I (ATT-I), which substantially promotes tumor antigen presentation of both human and mouse colorectal cancer (CRC) cells and thereby enhances the cytotoxic response of CD8⁺ T cells. Cellular thermal shift assay (CETSA) with multiplexed quantitative mass spectrometry identified the proteasome 26S subunit non-ATPase 4 (PSMD4), an essential component of the immunoproteasome complex, as a primary target protein of ATT-I. Binding of ATT-I with PSMD4 augments the antigen-processing activity of immunoproteasome, leading to enhanced MHC-I-mediated antigen presentation on cancer cells. In syngeneic mouse CRC models and human patient-derived CRC organoid models, ATT-I treatment promotes the cytotoxicity of CD8⁺ T cells and thus profoundly enhances the efficacy of immune checkpoint blockade therapy. Collectively, we show here that targeting the function of immunoproteasome with ATT-I promotes tumor antigen presentation and empowers T cell cytotoxicity, thus elevating the tumor response to immunotherapy.

Introduction

Current cancer immunotherapy is based on the longstanding immune surveillance hypotheses originating from the beginning of the 20th century. Regardless of diverse forms of cancer immunotherapy, they all share the common concept that the immune system is instructed to recognize and kill tumor cells. The immune system can distinguish healthy cells from tumor cells, as the latter expresses tumor associated antigens (TAAs). In the context of CD8⁺ T cell-mediated immune responses, recognition of TAAs occurs through the presentation of TAAs via MHC-I on tumor cells and their interaction with T cell receptor (TCR) on the CD8⁺ T cells. Impairing this event will ultimately reduce or annihilate the CD8⁺ T cell-mediated tumor cytotoxicity (1). However, reduction or loss of antigen presentation is a frequent and essential mechanism used by tumor cells to escape

immune recognition and destruction, including genomic deletion of MHC-I genes, transcriptional suppression of antigen presentation-associated genes, dysregulation of tumor antigen processing, and defective antigen transport to the cell surface and presentation (2–7). Conversely, increasing the presentation of antigen-loaded MHC-I complex on cancer cells renders them sensitive to T cell-mediated killing (7–9).

Rapid advances in cancer immunology led to several new immunotherapies that promote the strength of immune responses against tumors. They either stimulate the activities of specific immune responses or counteract immune suppression signals produced by cancer cells. In addition to therapeutic antibodies and immune system modulators, adoptive cell transfer and immune checkpoint inhibitors are among the most promising approaches in human cancer therapies (10, 11). However, despite the recent success in immunotherapies based on direct blockade of immune checkpoint proteins such as programmed death 1 (PD-1), cytotoxic T lymphocyte-associated protein 4 (CTLA-4) and programmed death ligand 1 (PD-L1), a majority of patients with solid tumors do not experience durable clinical responses. The mechanisms of tumor resistance against immune checkpoint blockade often involve low levels of tumor-infiltrating lymphocytes, suppressive immune cells (regulatory T cells, myeloid-derived suppressor

Authorship note: HX, KVDJ, and ZZ contributed equally to this work.

Conflict of interest: XL, XZ, and KVDJ submitted a patent (no. 63/122,232) for the method to sensitize cancer cells in immunotherapy using ATT-I.

Copyright: © 2021, American Society for Clinical Investigation.

Submitted: December 11, 2020; **Accepted:** April 7, 2021; **Published:** May 17, 2021.

Reference information: *J Clin Invest.* 2021;131(10):e146832.

<https://doi.org/10.1172/JCI146832>.

cells, and macrophages), and adverse tumor microenvironment (12–14). Analysis of longitudinal tumor biopsies from patients with immune checkpoint blockade therapies revealed a correlation of point mutations, deletions or loss of heterozygosity in the β -2-microglobulin (*B2M*) gene, which encodes an essential component of the MHC-I antigen presentation complex, with therapeutic resistance and poor clinical outcomes (2). Therefore, therapeutic intervention of tumor antigen presentation could be a promising option to improve responsiveness toward immune checkpoint blockade.

While MHC-II is normally restricted to antigen presenting cells (APCs) such as dendritic cells, macrophages, and B cells, the presentation of tumor-specific peptides on the tumor cells by MHC-I complex is critical to adaptive immune responses of CD8 $^{+}$ T cells. Generation of tumor antigens and their loading onto MHC-I involves multiple steps, in which all the components constitute the antigen processing and presenting machinery (APM). Tumor antigen processing starts from ubiquitination-associated immunoproteasomal activity that degrades tumor-specific proteins to peptides. Once transported into the endoplasmic reticulum by transporter associated with antigen processing (TAP), those peptides will be sorted by their length and sequence for selective loading onto the MHC-I (6). Aberrations in the APM genes are often found in human tumors and correlate with relevant clinical variables, including tumor grade, tumor stage, disease recurrence, and survival (15). Current findings suggest that defective APM is an important immune escape mechanism that prevents cytotoxic CD8 $^{+}$ T cells from recognizing tumor cells. Further understanding the regulation of APM is crucial for the optimization of T cell-based immunotherapy protocols.

Other therapeutic modalities such as radiation therapy and chemotherapeutics can induce bystander effects leading to the immunogenic tumor cell death, which in turn promotes cancer immunotherapy (16). However, one major drawback in those adjuvant treatments is their toxicity and adverse effects. Therefore, there is a need to find new therapeutic agents to promote the immune system with limited adverse reactions. Herbal medicines have accumulated tremendous amount of clinical experience over the years, in terms of their therapeutic efficacy, tolerance, and safety (17). However, in traditional herbal medicine therapies, their therapeutic efficacies are achieved by complex components rather than individual compounds with known chemical structure and targets. In most of the cases, it is unknown which active compound delivers therapeutic activity. Here, we investigated the potential application of purified herbal medicine compounds to improve colorectal cancer (CRC) immunotherapy and unravel their mechanisms of action. To this end, we screened a library of 594 small molecule compounds purified from traditional herbal medicine by their effects on the CD8 $^{+}$ T cell-mediated killing of CRC cells. Atractylenolide I (ATT-I) was identified as a new compound that substantially increases tumor antigen presentation and enhances the efficacy of CRC immunotherapy.

Results

The small-molecule compound ATT-I promotes CD8 $^{+}$ T cell-mediated tumor cell killing. To identify small molecular compounds for improving the CD8 $^{+}$ T cell-mediated killing of colorectal tumor cells in vitro, we screened a library containing 594 small-molecule

compounds purified from over 500 herbal medicinal plants that have been widely used in traditional Chinese medicine (Supplemental Table 1; supplemental material available online with this article; <https://doi.org/10.1172/JCI146832DS1>). The screen system includes the coculture of a mouse colorectal tumor cell line MC38 stably expressing the full-length chicken ovalbumin (OVA) together with enriched CD8 $^{+}$ T cells from the spleen of OT-I mice (C57BL/6-Tg(TcraTcrb)1100Mjb/J). OTI CD8 $^{+}$ T cells recognize the MHC class I-restricted OVA_{257–264} peptide. To exclude the compounds with high cytotoxic activity similar to that of chemotherapeutic drugs, we first assessed their cytotoxicity on both the CD8 $^{+}$ T cells and tumor cells (Figure 1A and Supplemental Table 1). The 449 compounds with minimum to low cytotoxicity on both T and tumor cells (>80% of viability in vehicle-treated cells) were sorted out for the next screen of antigen-specific OT-I CD8 $^{+}$ T cell killing of MC38-OVA tumor cells using an in vitro luciferase assay. Three top-ranked compounds that most potently affected the T cell activity are icariin, biochanin A, and ATT-I (Figure 1, B and C, Supplemental Figure 1, A and B, and Supplemental Table 2). Their activities were validated in the T cell cytotoxicity assays with the ratios of T cells versus tumor cells ranging from 5:1 to 1:5 (Figure 1D and Supplemental Figure 1, C and D). As ATT-I exhibited the most potent activity, we chose to further identify its mechanism of action. Upon pretreatment of either CD8 $^{+}$ T cells or the tumor cells separately, we found that ATT-I enhanced tumor-killing effects through modulation of tumor cells, but not CD8 $^{+}$ T cells as the treatment of CD8 $^{+}$ T cells only did not have notable effect on their cytotoxicity (Figure 1, E and F). To further confirm the activity of ATT-I, we generated 3D tumor organoids derived from MC38-OVA tumors and cocultured them with OT-I cells (Figure 2A). With the treatment of ATT-I, the tumor organoids exhibited markedly enhanced killing from the OT-I cells in comparison with that of the untreated organoids (Figure 2, B and C). However, this treatment had no notable effect on the organoids without addition of OT-I cells. Collectively, the results suggest that the ATT-I treatment increases the immunogenicity of the tumor cells.

ATT-I interacts with the immunoproteasome component PSMD4. ATT-I is one of the major bioactive ingredients isolated from the rhizomes of *Atractylodes macrocephala*. Previous studies have reported various pharmacological activities of ATT-I, including antiinflammation, neuroprotective activity, and anti-tumor activity (18, 19). However, due to lack of in-depth analysis and validation of these bioactivities, molecular targets of ATT-I and relevant mechanisms of action have yet to be determined. According to the chemical structure of ATT-I, it is technically difficult to identify its protein targets by direct biochemical methods such as affinity pull-down assay. Here, we conducted a mass cytometry screening assay based on melt temperature shifts, referred to as cellular thermal shift assay (CETSA), on MC38 tumor cells treated with or without ATT-I (Figure 3, A–D, Supplemental Figure 2A) (20). The CETSA approach is established on the same principle as conventional thermal shift assays. In this assay, potential target proteins of a small molecule compound display an altered melting curve when exposed to increased temperature. Thus, analysis of thermal stabilization or destabilization of total proteins in the cell allows us to identify the potential binding proteins of the small molecule compound. Control and

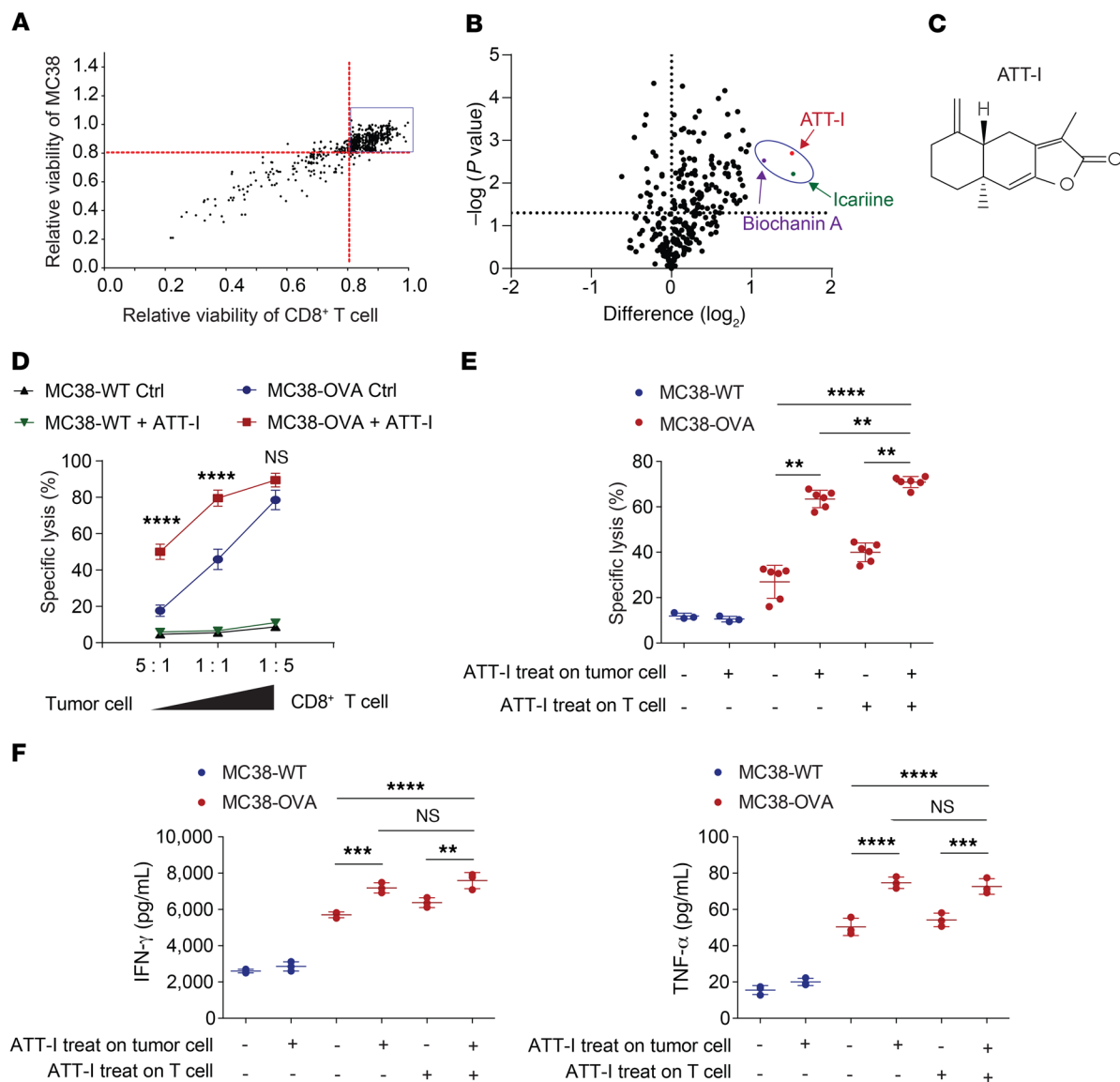


Figure 1. ATT-I enhances the killing efficiency of CD8⁺ T cells against tumor cells. (A) A total of 594 natural small molecule compounds purified from traditional medicinal plants were tested for their toxicity on MC38 cells and T cells freshly isolated from C57BL/6 mice. Data are presented as mean of 3 independent experiments. (B) The 446 drugs with low toxicity from (A) were tested for their effects on the CD8⁺ T cell-mediated cytotoxicity. MC38-OVA cells expressing luciferase were cocultured with OT-I CD8⁺ T cells in the presence of each drug (5.0 μ M) and the T cell-mediated cytotoxicity was measured by the luciferase assay. Difference (\log_2): (\log_2 [relative viability] > 1; $P < 0.05$). Relative viability = (tumor cell viability of treated group) / (tumor cell viability of control group). Data are presented as mean of 3 independent experiments. Statistical analysis was conducted using 1-way ANOVA. (C) Chemical structure of ATT-I. (D) The effect of ATT-I treatment on the CD8⁺ T cell killing of MC38-OVA cells was measured under different ratios of tumor cells versus T cells as indicated. Data are presented as mean \pm SD of 3 independent experiments. Statistical analysis was conducted using 2-way ANOVA. (E) CD8⁺ T cell killing assays were conducted using coculture of MC38-OVA cells and OT-I CD8⁺ T cells pretreated with 5 μ M of ATT-I (+) or vehicle control DMSO (-). Data are presented as mean \pm SD of 3 independent experiments. (F) The levels of IFN- γ (left) and TNF- α (right) in the supernatants after coculture of OT-I T cells and MC38-OVA cells pretreated with ATT-I (+) or DMSO control (-) were determined by ELISA. Data are presented as mean \pm SD of 3 independent experiments. Statistical analyses were conducted using 2-way ANOVA. *** $P < 0.01$; *** $P < 0.001$; **** $P < 0.0001$.

ATT-I-treated MC38 tumor cell lysates were heated to different temperatures (32°C to 75°C). Detectable proteins in the soluble fraction of cell lysates were quantified by mass spectrometry and their respective melting curve shifts were determined (Figure 3, A and B). Among the top potential protein targets (CGGBP1, SORBS3, COPB1, and PSMD4) identified from the screening assay, we validated PSMD4 as a primary target protein of ATT-I from its protein denaturation curves and thermal shift (Figure 3,

B-D). The proteasome 26S subunit non-ATPase 4 (PSMD4) is an essential component of the 19S regulator lid in the 26S immunoproteasome complex that processes MHC-I-associated antigen peptides (21-23). In the immunoproteasome, PSMD4 acts as an ubiquitin (Ub) receptor that mediates recruitment of the ubiquitylated protein for degradation and antigen processing (24). The altered protein stability and thermal shift of PSMD4 were further validated by Western blotting assay on mouse (MC38) and

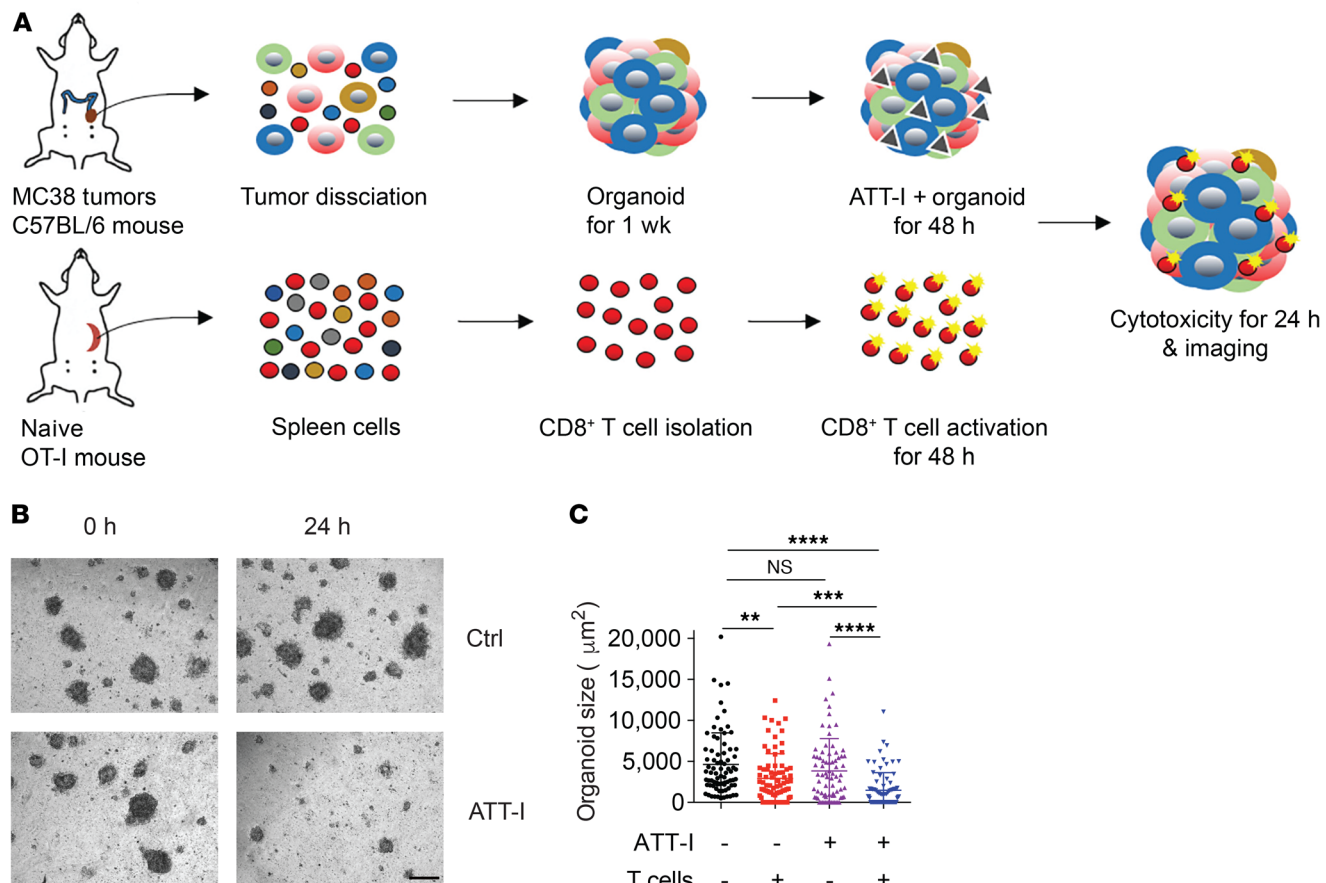


Figure 2. ATT-I enhances the antigen-specific T cell responses in MC38 tumor-derived organoids. (A) Schematic representation of the MC38-OVA-derived organoid killing assay. OT-I CD8⁺ T cells were cocultured with tumor organoids generated from MC38-derived tumors in C57BL/6 mice with or without ATT-I treatment. (B) Representative figures of MC38-derived tumor organoids taken at the indicated timepoints from the same well with control or ATT-I treatment. Scale bar: 100 μm . (C) Quantification of the organoid size presented as mean \pm SD of 3 parallel experiments. The size of organoids was measured as project area (μm^2) using Image J software. Statistical analysis was conducted using 2-way ANOVA. ** $P < 0.01$; *** $P < 0.001$; **** $P < 0.0001$.

human (HCT116) CRC cells, which showed enhanced PSMD4 protein stability upon ATT-I treatment (Figure 3E and Supplemental Figure 2B). To confirm the direct interaction of ATT-I with PSMD4, bacterially expressed mouse PSMD4 was purified and incubated with ATT-I under varying concentrations in the microscale thermophoresis (MST) binding assay. The results showed a notably high affinity of ATT-I to PSMD4 ($K_d = 0.4 \mu\text{M}$) (Figure 3F and Supplemental Figure 2C).

ATT-I promotes the activity of immunoproteasome in a PSMD4-dependent manner. The catalytic 20S core of the immunoproteasome is built from 2 outer α -rings and 2 inner β -rings that are composed of α -subunits and β -subunits, respectively, as illustrated in Figure 4A. The immunoproteasome can come in several variants containing the 20S core alone, or with 1 or 2 regulatory lids (25). The 19S regulatory cap is essential to recognize and unfold polyubiquitinated proteins. The 19S is composed of ATPase (RPT) and non-ATPase (RPN) subunits including PSMD4 (Figure 4A). Structural analysis of the PSMD4-containing human 26S proteasome predicted a potential binding site near the Cys58 group of PSMD4 for ATT-I (Figure 4, B-D). To highlight the interaction of ATT-I with neighboring amino acids on PSMD4, we generated a ligand interaction diagram. The diagram was generated

using the covalent complex between ATT-I and PSMD4, as shown in Figure 4D. In the covalent complex, the ATT-I compound engages PSMD4 primarily through hydrophobic interactions with Val-60 and Val-92. To get deeper insight into the strength of the interaction between ATT-I and PSMD4, a molecular mechanics calculation, Generalized-Born, and surface area calculation (MM-GBSA) were carried out using the Prime module of the Schrodinger molecular modeling package. The MM-GBSA energy determines the contributions of electrostatics and nonpolar interactions to the free energy. It was determined for the noncovalent complex between ATT-I and PSMD4. The total MM-GBSA energy for ATT was -18 kcal/mol, with -5 kcal/mol contribution from the electrostatic component, which includes Coulomb energy and polar solvation energy, and -13 kcal/mol from the nonpolar component, which includes van der Waals and nonpolar solvation. This confirms that the binding affinity of ATT-I to PSMD4 is primarily driven by nonpolar hydrophobic interactions.

We wanted to see if ATT-I promotes the activity of the immunoproteasome in the antigen processing in cancer cells. To verify the activity of ATT-I on the 26S immunoproteasome, we assessed the chymotrypsin-like, trypsin-like and caspase-like activities on the lysates of MC38 cells treated with or without ATT-I. The

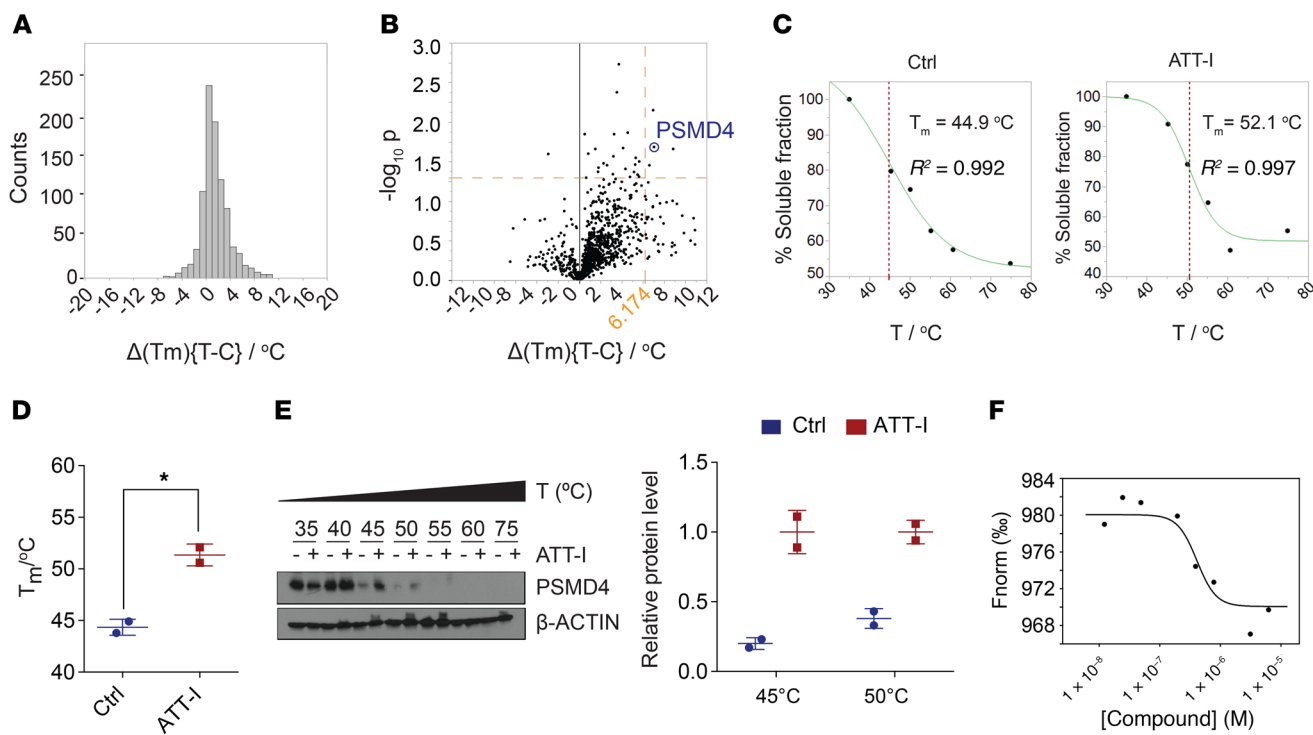


Figure 3. PSMD4 is identified as a molecular target of ATT-I in the immunoproteasome. (A–D) Cellular thermal shift assay was conducted to identify potential molecular targets of ATT-I in MC38 cells using melting temperature (T_m) shifts. (A) Distribution plots of $\Delta(T_m)$ values for proteins from control and ATT-I-treated cells. (B) Volcano plots of $\Delta(T_m)$ values to identify potential targets of ATT-I with the most significant melting temperature changes. PSMD4 is indicated on the plots. (C) Temperature based protein-nondenaturation curves for PSMD4 in control and ATT-I-treated cell lysates. (D) Quantitative data from (C) are presented as mean \pm SD of 2 parallel experiments ($n = 2$). Unpaired 2-tailed *t* test was used for statistical analysis. (E) Representative immunoblots of PSMD4 in the MC38 cell lysates with or without ATT-I treatment are shown. (F) Microscale thermophoresis (MST) binding assay determined the K_d value ($K_d = 0.4 \mu\text{M}$) for the binding of ATT-I toward PSMD4. Data shown are representative of 4 independent experiments. * $P < 0.05$.

Ac-ANW-AMC (chymotrypsin substrate), Ac-PAL-AMC (trypsin substrate), and Ac-KQL-AMC (caspase substrate) substrates were incubated with the cell lysates and their cleavage activities were measured by the released AMC fluorescence. The ANW and PAL are preferred substrates for the immunoproteasome while KQL can be cleaved by both the immunoproteasome and constitutive 26S proteasomes. The ATT-I treatment led to markedly enhanced activities of the immunoproteasome in processing all the 3 types of substrates. However, knockdown of *PSMD4* in the cell abolished the effect of ATT-I, suggesting the ATT-I activity on the immunoproteasome is dependent on PSMD4 (Figure 4D and Supplemental Figure 2D). Due to the spatial proximity of PSMD4 and PSMD7 in the immunoproteasome, we reasoned that their interaction is essential for the activity of immunoproteasome. Indeed, knockdown of either PSMD4 or PSMD7 reduced the biochemical activity of the immunoproteasome in the cell lysates (Figure 4E). However, no difference on cell proliferation was observed in the cancer cells with PSMD4 or PSMD7 knockdown as compared with their control cells expressing nontargeting shRNAs (shNT) (Supplemental Figure 3, A and B), consistent with the notion that the immunoproteasome function is dispensable for cell survival and growth. The interaction of PSMD4 and PSMD7 seemed to be enhanced after ATT-I treatment, as shown in the results of immunoprecipitation and Western blotting analyses. In the PSMD4-containing immunoprecipitates, an increased level of PSMD7 proteins was detected in the cell lysates with ATT-I

treatment (Supplemental Figure 3C). Together, these data suggest that ATT-I enhances the immunoproteasome activity via its interaction with PSMD4.

ATT-I promotes antigen presentation and enhances the efficacy of CRC immunotherapy. We demonstrated enhanced cleavage activity of the protease substrates by the immunoproteasome upon ATT-I treatment. Consequently, this enhanced immunoproteasome activity could ultimately promote antigen processing and presentation on tumor cells. Tumor antigen presentation to CD8⁺ T cells is mediated by the MHC class I complex. We thus assessed the levels of MHC-I on the surface of mouse (MC38, CT26) and human (HCT116, SW837) CRC cells. The result showed that both mouse and human tumor cells displayed increased levels of MHC-I (H-2Kb and H-2Kd for MC38 and CT26, respectively, and HLA-A,B,C for HCT116 and SW837) on the cell surface, indicating increased antigen presentation on the ATT-I-treated tumor cells (Figure 5, A–C and Supplemental Figure 4A). In order to confirm that the modulation of cytotoxicity is due to the MHC-I/TCR interaction, we tested the effect of ATT-I on the cytotoxicity of MC38 OVA⁺ after blocking the MHC-I/TCR interaction using MHC-I (H2) antibody (Figure 5D). Our results suggest that after blocking the MHC-I/TCR interaction, the cytotoxicity effect was decreased as compared with the isotype control groups. Importantly, the effect of ATT-I on tumor cell killing was almost eliminated. Notably, the effect of ATT-I treatment on the enhanced antigen presentation was abrogated in the cells with PSMD4 or

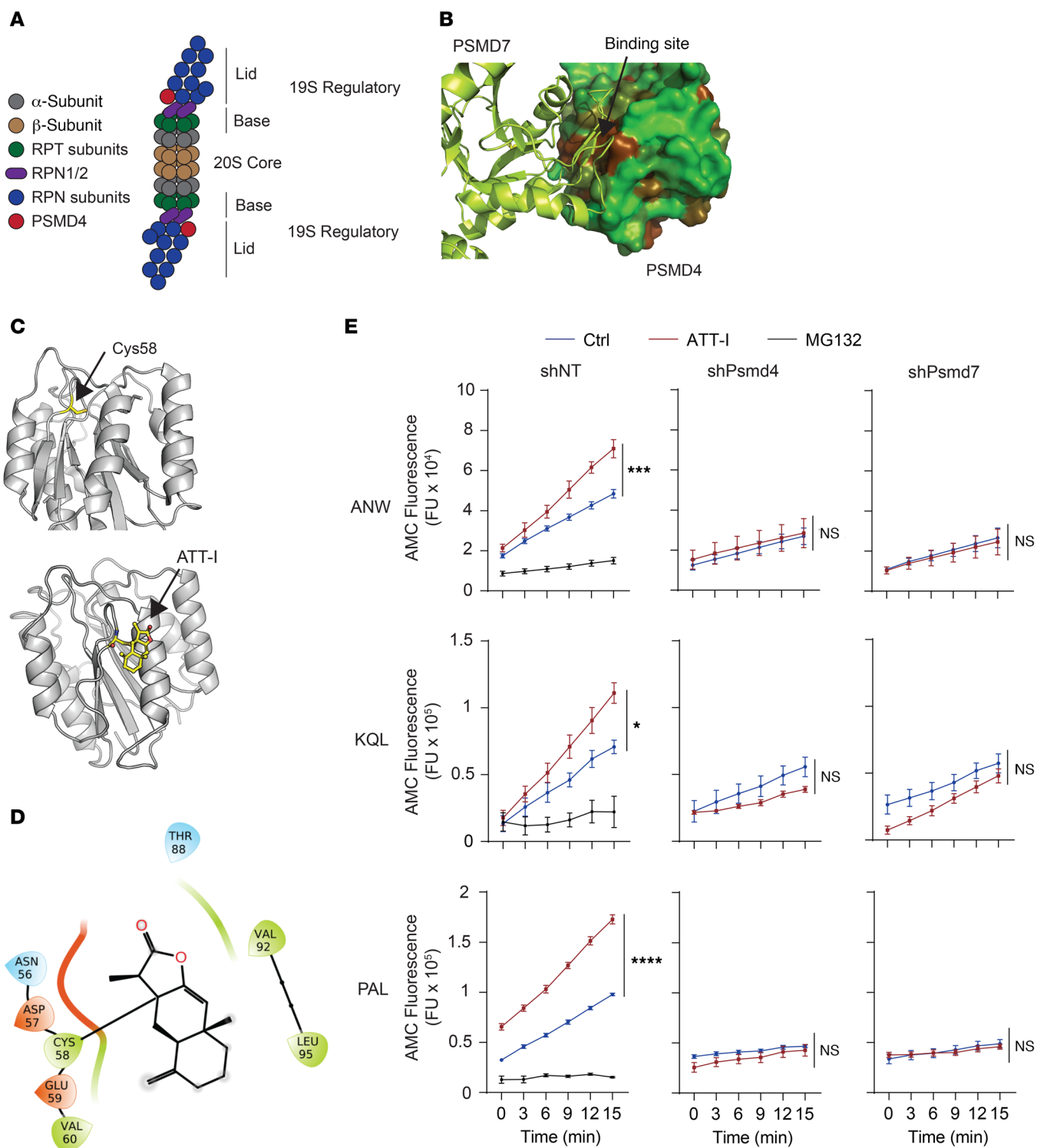


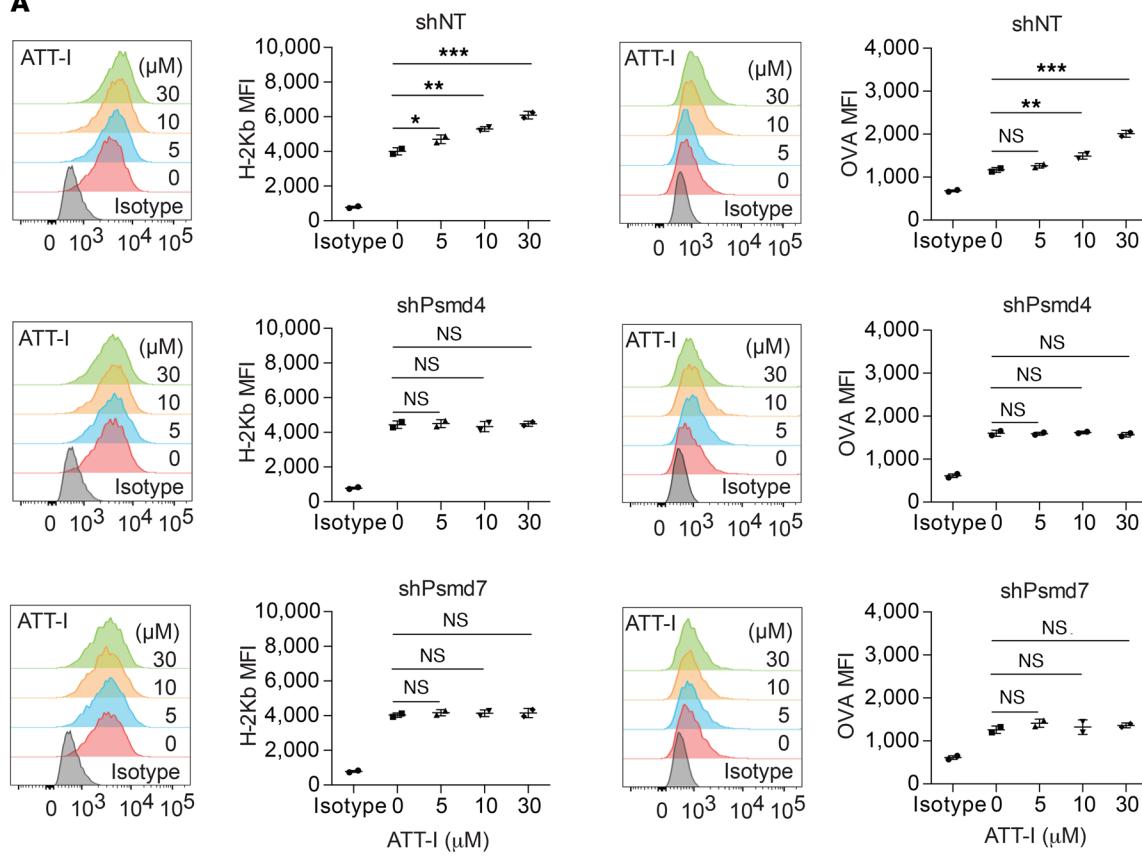
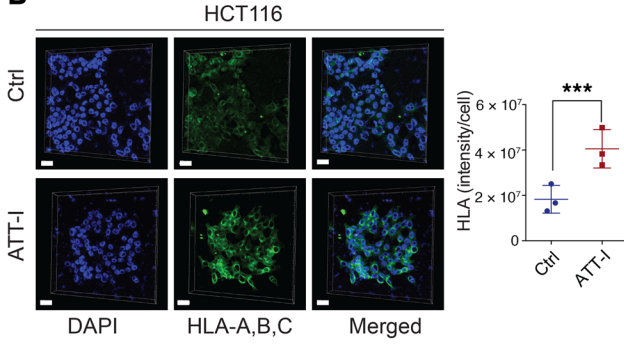
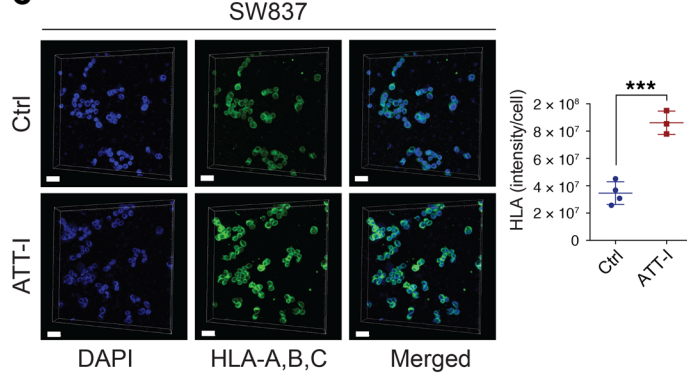
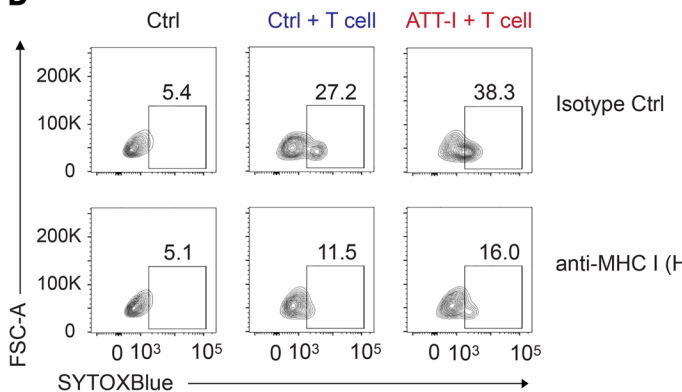
Figure 4. ATT-I binds to PSMD4 and stabilizes the PSMD4 and PSMD7 interaction, leading to enhanced proteasomal activities. (A) Schematic representation of the immunoproteasome. (B) Three-dimensional structure of the complex between PSMD4 and PSMD7 obtained from the cryo-EM structure of the 26S proteasome (PDB code 6EPD). PSMD4 is shown in solvent-accessible surface area, color-coded based on hydrophobicity (brown is hydrophobic and green hydrophilic). PSMD7 is shown in green ribbon representation. (C) Three-dimensional structure of PSMD4 shown in gray ribbon representation. The cysteine residue Cys58 located at the PSMD4 and PSMD7 interface is shown in capped-sticks rendering (upper panel). The predicted structure of the covalent complex between PSMD4 and ATT-I (bottom panel). PSMD4 is shown in gray ribbon rendering, and Cys-58 and ATT-I are depicted in capped-sticks representation (yellow, red, blue, and gold correspond to carbon, oxygen, nitrogen, and sulfur, respectively). (D) Ligand interaction diagram showing individual interaction of ATT with neighboring amino acids on PSMD4. (E) Activity analysis of immunoproteasomes purified from control or PSMD4-knockdown MC38 cell lysates upon treatment with ATT-I using different substrates (ANW, KQL, and PAL) as indicated. Quantitative data are presented as mean \pm SD of 2 parallel experiments ($n = 2$). Statistical analysis was conducted using 2-way ANOVA. * $P < 0.05$; *** $P < 0.001$; **** $P < 0.0001$.

PSMD7 knockdown (Figure 5A). Because CD8⁺ T cells recognize tumor cells through the interaction of MHC-I with the TCR, we reasoned that the enhanced tumor cell recognition would improve the efficacy of the anti-PD-1-based immunotherapy. We therefore assessed the therapeutic responses of CRC tumors to the combinational treatment of PD-1 mAbs with ATT-I (50 mg/kg) in C57BL/6 and BALB/c mice bearing MC38- and CT26-derived tumors, respectively (Figure 6, A–C and Supplemental Figure 4, C and D). As for the clinical context, MC38-derived colorectal tumors with high microsatellite instability (MSI-H) responded better to anti-PD-1 treatment, whereas CT26 tumor-bearing mice, a model for microsatellite stable (MSS) tumors, displayed a low anti-PD-1 therapeutic benefit (26). Interestingly, in both cases, the addition of ATT-I to the PD-1 blockade treatment resulted in marked tumor growth control, while the ATT-I treatment by itself only had modest effects. The results suggested that ATT-I treatment may promote global antigen presentation of tumor cells regardless of the amounts of tumor neoantigens in MSI-H and MSS tumor cells. Additionally, due to the immunosuppressive tumor microenvironment, CD8⁺ T cells are often found at inactive states, which can be activated by the PD-1 inhibition for better killing of the tumor cells with enhanced antigen presentation (12). We further validated the enhanced therapeutic benefit for the combination of ATT-I with the PD-1 blockade in the orthotopic MC38 tumor model (Figure 6, D and E) (14). While the PD-1 mAb treatment notably extended the survival of the tumor-bearing mouse (median survival time, 50 days) in comparison with the control mice (median survival time, 29 days) or the mice treated only with ATT-I (median survival time, 34 days), the combination of PD-1 mAb and ATT-I further extended the survival of the tumor-bearing mice with median survival time greater than 140 days. Consistent with previous studies regarding the biosafety of *Atractylodes macrocephala* (1.32 g daily for up to 7 weeks) in clinical applications, treatment of ATT-I at the tested doses had no notable toxicity in vivo (27). Animal body weights and pathological analysis of major organs did not reveal any substantial differences between the ATT-I-treated group and the control vehicle group (Supplemental Figure 5), suggesting negligible systemic toxicity of ATT-I. To determine whether the specific targeting of ATT-I on PSMD4 enhanced the therapeutic responses of PD-1 blockade, we treated the mice harboring MC38-PSMD4^{loss} tumors with anti-PD-1 only or anti-PD-1 in combination with ATT-I (Figure 6F). The additional benefit from ATT-I in combination therapy completely disappeared, hereby confirming the specific action of ATT-I through targeting PSMD4.

ATT-I enhances CD8⁺ T cell infiltration and cytotoxicity in CRC immunotherapy. As ATT-I promotes the antitumor immune responses in immune checkpoint blockade therapy, we next wanted to define the effects of ATT-I treatment on the immunological changes in CRC tumors. To this end, we harvested colorectal tumors 28 days after orthotopic cecal wall implantation of MC38 cells for the analysis of tumor microenvironment using mass cytometry (CyTOF) (Figure 7A and Supplemental Table 3). Similar to the tumor growth studies mentioned above, the ATT-I treatment significantly enhanced the antitumor effects of PD-1 mAb treatment (Figure 7B). The combination of PD-1 mAb and ATT-I led to a drastically enhanced T cell infiltration and reduced macrophage infiltration in comparison with single agent treatments of

either PD-1 mAb or ATT-I (Figure 7, C and D and Supplemental Figures 6 and 7), thereby tipping the balance toward a more anti-tumor microenvironment. Although we do not assume any direct effect of ATT-I on macrophages, their reduced infiltration could be a reflection of the general immune response in situ. This phenomenon could be explicated by an enhanced cytotoxicity of CD8⁺ T cells, as they secrete several cytokines that could reduce the infiltration and inflammation, thereby leading to a lower number of macrophages in the tumor microenvironment. Further analysis revealed that both CD8⁺ and CD4⁺ T cells displayed lower CD69 expression levels upon the combination of ATT-I with anti-PD-1 (Supplemental Figure 6K). The reduced expression levels of CD69 may account for a rescue from T cell exhaustion, which is also reflected by their enhanced capacity to secrete interferon gamma (IFN- γ) (Supplemental Figure 6J and ref. 28). To determine the immune cell population responsible for the antitumor effect of ATT-I, we depleted mice of B cells, CD4⁺ T cells, or CD8⁺ T cells (Figure 7, E–G). The depletion antibodies were administered intraperitoneally before tumor inoculation and every 3 days thereafter until the end of the experiment. The antitumor effect for the combination of ATT-I with PD-1 mAb was completely abrogated upon CD8⁺ T cell depletion. By contrast, depletion of CD4⁺ T cells had no notable effect, whereas B cell depletion only minimally reduced the antitumor effects. As the main effects of ATT-I were mediated through CD8⁺ T cells, we next applied single-cell RNA sequencing (scRNA-seq) analysis of colorectal tumor samples from the mice treated with control, ATT-I, PD-1 mAb, or ATT-I + PD-1 mAb, to further assess the CD8⁺ T cell functions under each conditions. In the t-SNE plot analysis of the scRNA-seq data, types of cells in the tumors were assessed by their gene expression signatures (Figure 8, A and B). We determined the expression levels of T cell activation (Cd8a, Icos, Cd28, Cd44, and Cd69) and cytotoxicity (Ifng, Prf1, Pdcd1, and Sla2) genes in the tumors with each treatment (Figure 8C). Our data in general confirm the enhanced activation and cytotoxicity of the combination treatment of ATT-I and PD-1 mAb (Figure 8D). Cytotoxicity levels in the combination treatment group displayed a significant increase in highly cytotoxic CD8⁺ T cells (Figure 8E). The data together with the functional capacity of CD8⁺ T cells in the combo treatment group to secrete higher levels of IFN- γ (Supplemental Figure 6J) and the depletion experiment (Figure 7, F and G) confirm the critical role of CD8⁺ T cells in the antitumor immune responses upon the treatment of ATT-I and PD-1 mAb.

Next, we applied a total of 8 patient-derived tumor organoids (PDOs) from freshly resected tumor tissues to determine whether treatment of tumor organoids with ATT-I affects the cytotoxicity of autologous CD8⁺ T cells from the same tumor tissue (Figure 9A and Supplemental Table 4). After tumor dissociation, tumor cells were mixed with adherent stromal cells (fibroblasts, endothelial cells, and macrophages) to form PDOs. When the organoids reached 100 μ m in diameter, they were cocultured with the pre-activated autologous CD8⁺ T cells isolated from the same tumor tissue. Spheroid dissociation and T cell cytotoxicity were assessed (Figure 9, B and C and Supplemental Figure 8). As expected, the ATT-I-treated PDOs became more vulnerable to CD8⁺ T cell killing as compared with the control PDOs, indicated by markedly high levels of organoid dissociation (Figure 9, B and C and Supple-

A**B****C****D**

- (Ctrl) MC38 OVA⁺
- (Ctrl) MC38 OVA⁺ + T cell
- (ATT-I) MC38 OVA⁺ + T cell

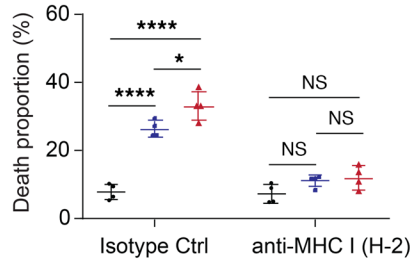


Figure 5. ATT-I enhances antigen presentation on tumor cells. (A) MFI values of H-2Kb and H-2Kb-SIINFEKL (OVA) on the MC38-OVA cells (shNT control, shPsmd4, and shPsmd7) with ATT-I (0, 5, 10, and 30 μ M), which were determined by flow cytometry analysis. Data are presented as mean \pm SEM and are representative of 2 independent experiments ($n = 2$). Statistical analysis was conducted using 1-way ANOVA. (B and C) HLA-A,B,C on the surface of HCT116 cells (B) and SW837 cells (C) was analyzed by 3D confocal imaging of immunofluorescence. Cell nucleus was stained by 4',6-diamidino-2-phenylindole (DAPI). Quantitative data are presented as mean \pm SD of 3 to 4 parallel experiments ($n = 3$ –4). Unpaired 2-tailed *t* test was used for statistical analysis. Scale bars in B and C: 30 μ m. (D) The effect of ATT-I on the cytotoxicity of MC38 OVA⁺ after blocking the MHC-I/TCR interaction using the MHC-I antibody. Specifically, we treated MC38 OVA⁺ cells with and without 30 μ M ATT-I for 48 hours. Rat IgG2a isotype control and anti-mouse MHC class I (H2) were used for blocking the cells overnight. The antigen-specific cytotoxicity was analyzed by flow cytometry. Data are presented as mean \pm SEM and are representative of 2 independent experiments ($n = 4$). Statistical analysis was conducted using 1-way ANOVA. **P* < 0.05; ***P* < 0.01; ****P* < 0.001.

mental Figure 8C) and tumor cell death (Supplemental Figure 8, A and B). Collectively, the results of the *in vivo* and *ex vivo* studies suggest that ATT-I treatment further empower immune checkpoint blockade therapy in treating CRC by promoting T cell infiltration and cytotoxicity.

Discussion

In addition to conventional chemotherapy and targeted therapy, immune checkpoint inhibitors have now entered into clinical care for CRC with deficient mismatch repair. However, positive responders to the immune checkpoint blockade therapies are only limited to a small subset of patients with MSI-H that encompasses approximately 5.9% of total CRC patients (29, 30). Even in this limited number of cases, not all patients respond to the treatment (31). Because MSS CRC with proficient mismatch repair does not respond to single-agent checkpoint blockade, new strategies have been evaluated for combinations with chemotherapy, vaccines, immune modulation, depletion of myeloid-derived suppressor cells, and suppression of regulatory T cells. While most of the immunotherapies are deemed to increase the activity of cytotoxic T lymphocytes (CTLs), it is noteworthy that cancer cells can be killed by the CTLs only if their tumor antigens are presented and recognized. Not surprisingly, cancer cells have developed a number of mechanisms to evade immune attacks by molecular evolution in tumor progression. A frequent mechanism for immune evasion is genomic deletion or suppressed expression of genes responsible for the MHC-I-mediated antigen presentation. Deletion of MHC-I genes, HLA, and B2M genes is often found in a number of human cancers. However, in colorectal cancer, fewer than 7% of cases harbor these hard lesions (5% B2M lesions and less than 2% HLA lesions based on the analysis of TCGA colorectal cancer datasets). Colorectal tumors with functional MHC-I genes can suppress tumor antigen processing and presentation through low immunoproteasome activity, deficient antigen loading on the MHC-I complex, and dysregulated antigen-MHC-I complex presentation. Although this mechanism is independent of alterations in the tumor microenvironment that could impact the attraction of T cells to the tumor, it would ultimately impede proper tumor cell recognition and killing by T cells.

Instead of identifying unique neoantigens from each tumor, upregulation of antigen processing and presentation on tumor cells seems to be a promising approach to enhance the efficacy of most immunotherapies. Antigen processing machinery has been studied mostly in terms of their structure, components, and molecular interactions (32). However, due to its complexity, modulation of the immunoproteasome activity is poorly understood. Proinflammatory cytokines (interferons and tumor necrosis factor α) as well as nitric oxide have been reported to induce the expression of immunoproteasome genes (33). Here, we explore the advantage to enhance therapeutic efficacy of PD-1 checkpoint immunotherapy with ATT-I, a small molecule that targets an essential component of the immunoproteasome, PSMD4. The ATT-I binding markedly increases the protease activity of the 26S immunoproteasome possibly through interfering with the PSMD4-PSMD7 interaction. The effect of ATT-I is presumably not limited to specific antigen processing or specific types of cancer cells, as PSMD4 is an essential component of the immunoproteasome in any cancer cell. The immunoproteasome functions in other types of cells, such as T cells, may also be modulated by ATT-I. However, treatment of T cells with ATT-I seemed to have no notable effect on their cytotoxic activity, suggesting that ATT-I may primarily promote antigen presentation of tumor cells and their interaction with T cells. In this study, our results clearly show that ATT-I profoundly enhances the therapeutic efficacy of immune checkpoint blockade when combined with PD-1 inhibitor. Interestingly, a recent study reported that overexpression of the immunoproteasome subunits PSMB8 and PSMB9 was predictive for better melanoma patient survival and response rates to immune checkpoint inhibitors (34). However, no significant therapeutic effect was observed while using ATT-I with the dose of 50 mg/kg as monotherapy. This was not unexpected since our drug screening method excluded potential targets affecting tumor cell viability (Figure 1A). Therefore, this suggests that ATT-I rather works as an adjuvant by improving tumor cell recognition.

The CETSA screen also identified Cggbp1, Sorbs3, and Copb1 as potential ATT-I targets. While biological functions of Cggbp1 and Sorbs3 and their association with tumor immunology remain unclear, Copb1, a protein subunit of the coatomer complex, is functionally associated with non-clathrin-coated vesicles (35, 36). The coatomer complex forms in the cytoplasm and is recruited to the Golgi where it assists in the intracellular trafficking of protein and lipid components to the endoplasmic reticulum (37). It will be interesting to see whether ATT-I promotes the trafficking of tumor proteins and their resulting antigens in the cell. While we provide strong evidence that PSMD4 is the target of ATT-I, we cannot rule out any off-target effects from ATT-I. Nevertheless, the critical validation for the improved benefit through the interaction of ATT-I with PSMD4 was provided that no additional benefit was observed for the combo-treated mice bearing PSMD4-silenced tumors. Moreover, our data suggest that ATT-I stabilizes the interaction of PSMD4 with PSMD7, hereby promoting the immunoproteasome activity and ultimately enhancing MHC-I tumor antigen presentation on the cell surface.

Using the CT26 mouse model, known to share genomic similarities to human MSS tumors that do not respond to immune checkpoint therapy, we also observed a therapeutic benefit in the combination group (26). This result suggests that we could poten-

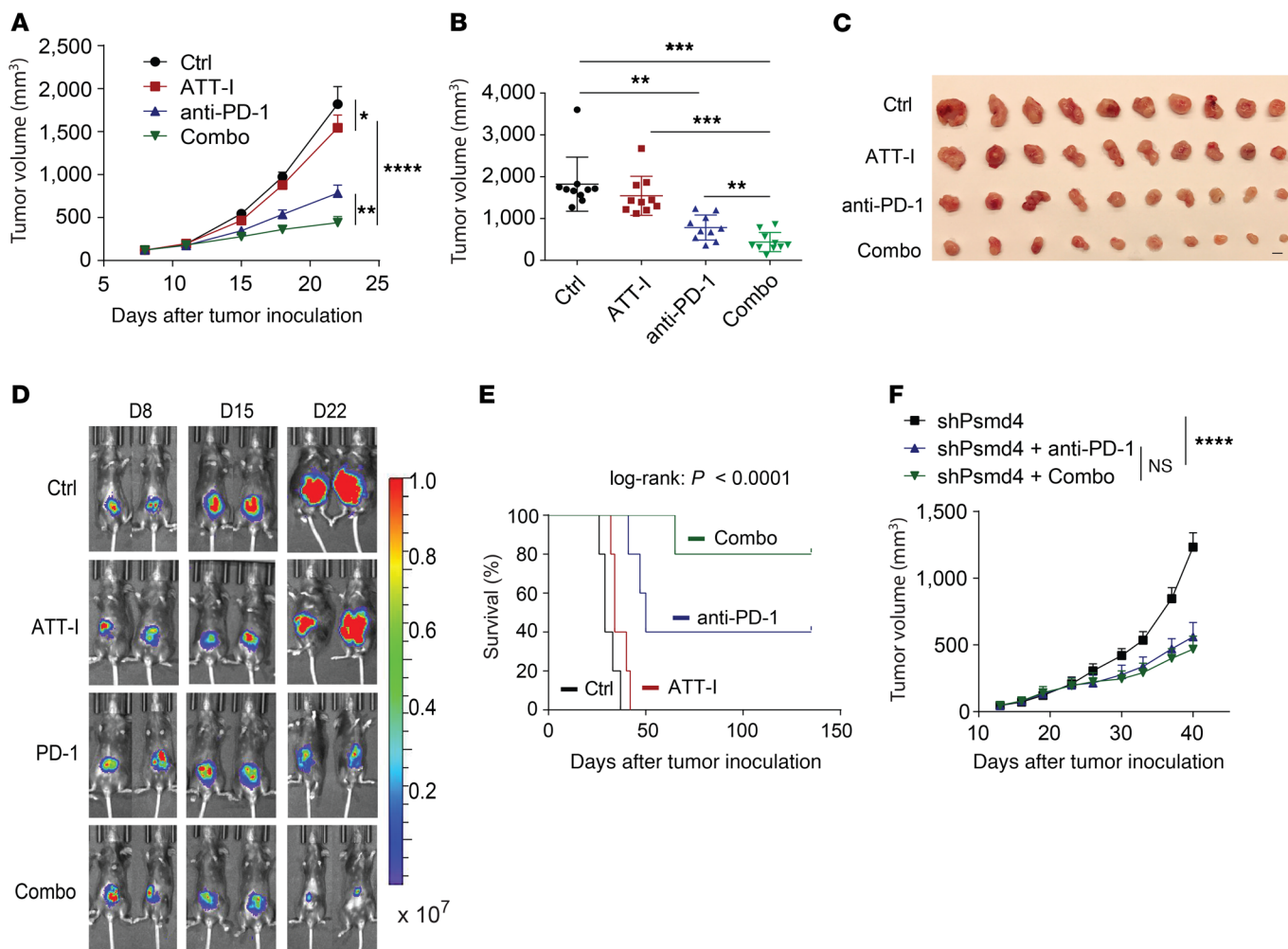


Figure 6. ATT-I enhances the immune checkpoint blockade immune responses. (A–C) Effects of the ATT-I (daily) and anti-PD-1 (3 times/week, 5 injections in total) on tumor growth (A) and tumor volume (B) of MC38-derived tumors in the subcutaneous C57BL/6 mouse model. Error bars represent SEM ($n = 10$ mice per group). Data shown are 1 representative of 2 independent experiments. Statistical analysis was conducted using 2-way ANOVA (A) and 1-way ANOVA (B). Pictures of the resected tumors (C). Scale bar: 1 cm. (D and E) Effects of the ATT-I (50 mg/kg, daily) and anti-PD-1 (200 μ g/mouse, 3 times/week, 5 injections in total) on tumor growth, measured via bioluminescence imaging (F) and survival (G) on the orthotopic MC38-derived tumor model (log-rank test). Each group includes 5 mice. (F) Tumor growth curves of MC38-derived tumors with or without PSMD4 knockdown and treated with anti-PD-1 only or anti-PD-1 together with ATT-I (combo). Each group includes 6 mice. Statistical analysis was conducted using 2-way ANOVA. * $P < 0.05$; ** $P < 0.01$; *** $P < 0.001$; **** $P < 0.0001$.

tially expand the number of CRC patients sensitive to checkpoint immunotherapy, which is a primary focus in clinical development (13). MSS colorectal tumors show an enrichment in heterozygous loss of chromosome 15 that contains the *B2M* gene (38). In addition, *B2M* mutations are identified solely in patients who did not respond to checkpoint immunotherapy (2). However, homozygous loss of *B2M* is quite rare (~3%) in CRC, suggesting that most colorectal tumors have a reduced amount of functional MHC-I complexes in the cell. Increasing the yield of antigens by ATT-I for presentation may be a potential approach to compensate for the partial loss of MHC-I complex.

In summary, the results of this study demonstrate that ATT-I, a small chemical compound from herbal medicine, is functionally associated with the immunoproteasome and thus promotes antigen processing and presentation on both checkpoint-sensitive and -resistant CRC tumors. This is important, as reduced immune response and immune evasion of tumor cells are major hurdles

in cancer immunotherapy. The treatment of ATT-I can sensitize CRC tumors to the immune checkpoint blockade therapy. Expanding these findings to different types of tumors such as melanoma and lung cancers warrants further investigation.

Methods

Mice and cell lines. C57BL/6 and BALB/c mice, 6 to 8 weeks old, were purchased from Jackson Laboratory and housed under pathogen-free conditions. OT-I mice (C57BL/6-Tg(TcrαTcrβ)1100Mjb/J) were purchased from Jackson Laboratory and bred in-house. All mice were housed in the animal facility of Indiana University School of Medicine. All procedures were carried out in accordance with approval of the Indiana University Institutional Animal Care and Use Committee protocol. The MC38 cell line was obtained from Patrick Hwu, MD Anderson Cancer Center and CT26, SW837, and HCT116 cell lines were obtained from ATCC. MC38, HCT116, and SW837 cells were maintained in DMEM supplemented with 10% FBS (Sigma-Al-

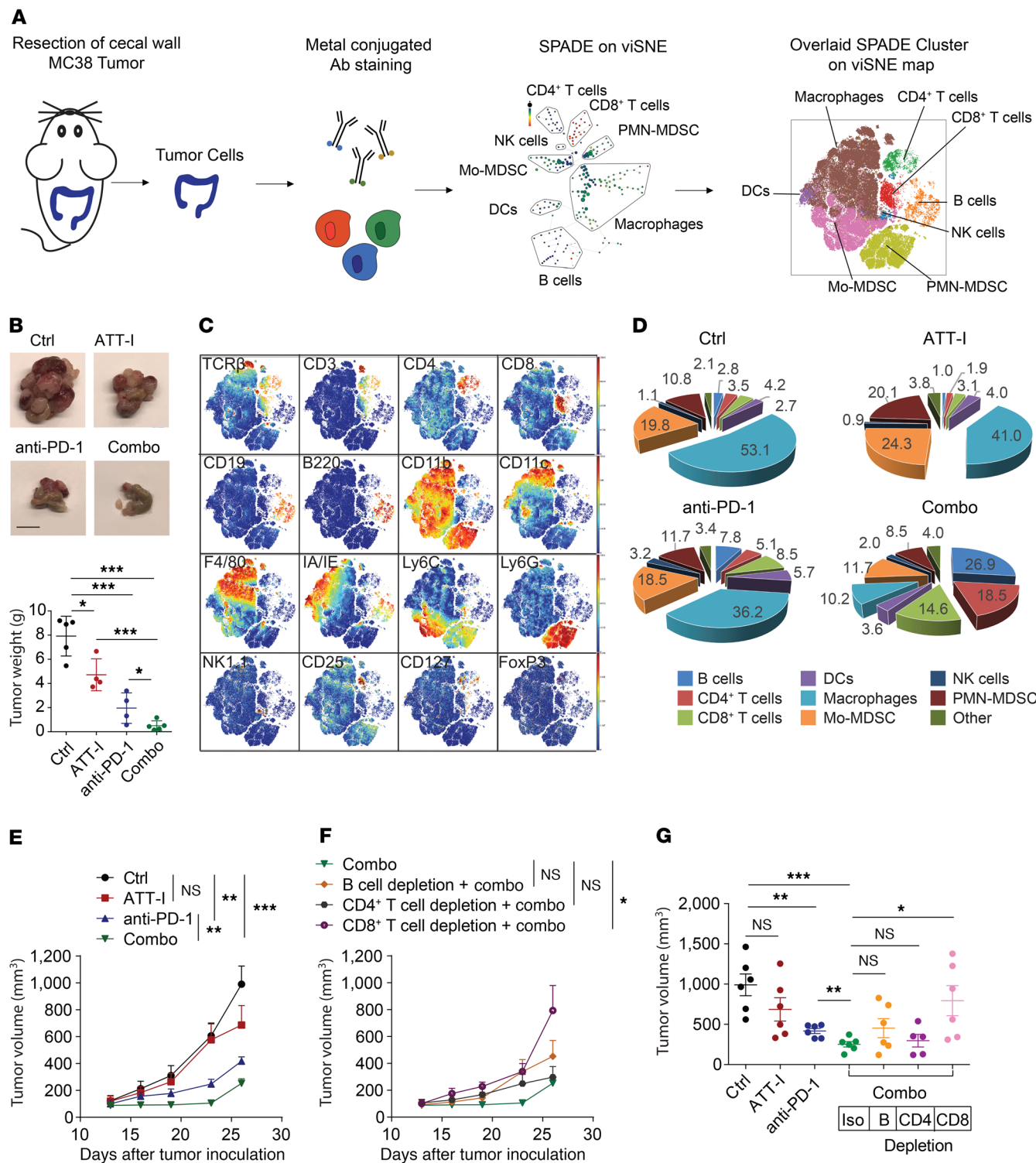


Figure 7. ATT-I enhances tumor-infiltrating lymphocytes and antitumor activity of cytotoxic T lymphocytes. (A) Schematic illustration of the immune composition analysis using single-cell mass cytometry (CyTOF). Orthotopic MC38 tumors were surgically resected, dissociated to single cells, and stained with metal isotope-conjugated antibodies. Immune profiles were assessed via CyTOF (26 markers) and analyzed using the Cytobank platform. viSNE analysis was performed, and thereafter SPADE on viSNE was assessed for an overlaid clustering of the immune cell populations. (B) Representative MC38 tumor images and weights of cecal wall implanted tumors ($n = 5$ in each group). Statistical analysis was conducted using 1-way ANOVA. Scale bar: 1 cm. (C) viSNE plots of the indicated markers used for the determination of the cell population gates. (D) Percentages of distinct immune cell populations within the CD45⁺ infiltrating immune cells in colorectal cancer tumors analyzed with Cytobank ($n = 5$). (E–G) Once the subcutaneous MC38 tumors were established, mice were randomly assigned into 7 groups and treated as indicated. Effects of the ATT-I (50 mg/kg, daily) and anti-PD-1 (3 times/week, 5 injections in total) treatment on tumor growth (E and F) and tumor volume (G) upon depletion of B cells, CD4⁺ T cells, and CD8⁺ T cells ($n = 6$). Error bars represent SEM and statistical analysis were conducted using 2-way ANOVA (E and F) and 1-way ANOVA (G). * $P < 0.05$; ** $P < 0.01$; *** $P < 0.001$.

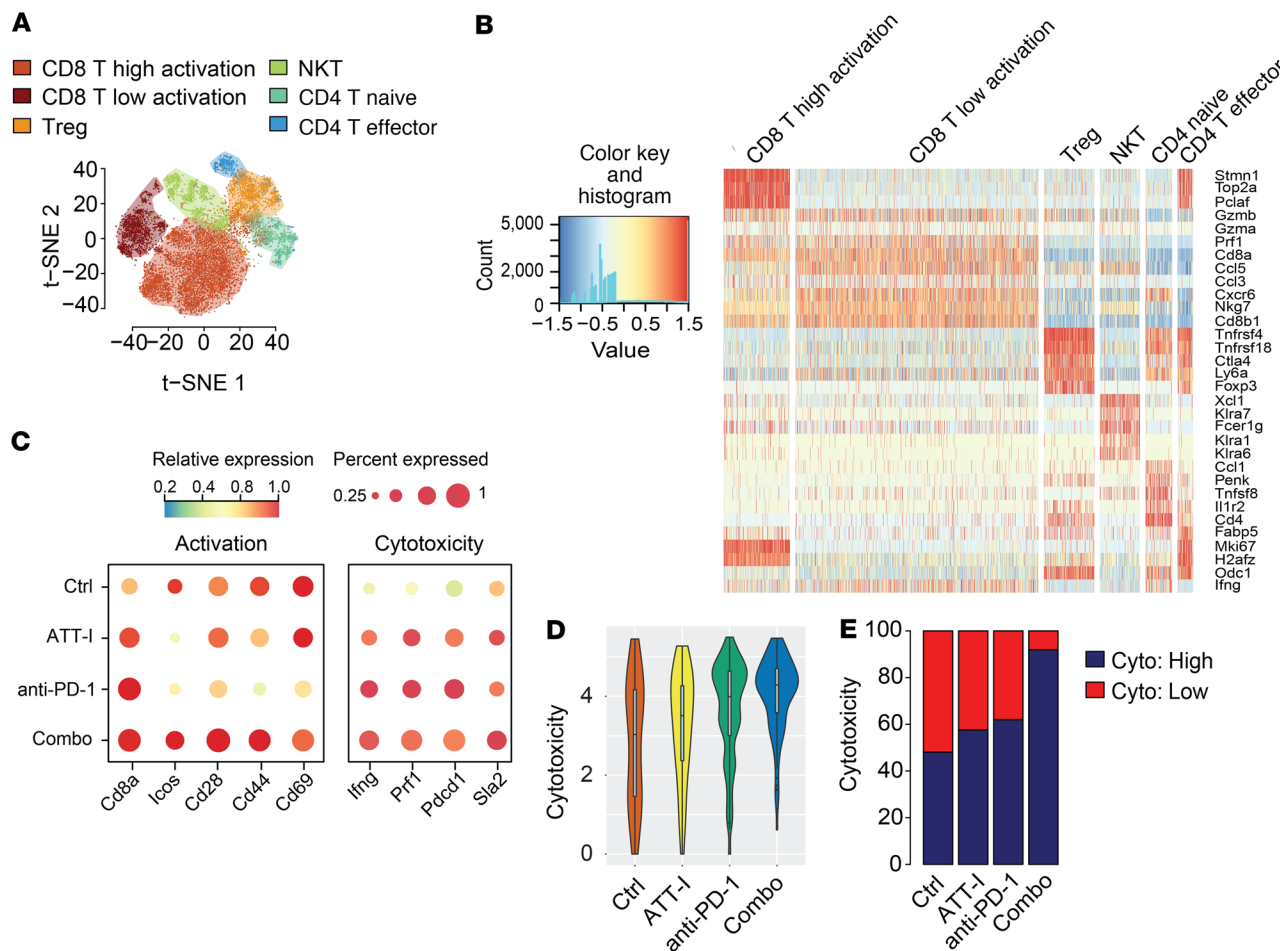


Figure 8. Single-cell RNA-seq analysis of mouse colorectal tumors treated with ATT-I in combination with immune checkpoint blockade therapy.

C57BL/6 mice bearing orthotopic implanted MC38-derived tumors were treated with vehicle control, ATT-I (50 mg/kg, daily), anti-PD-1 (3 times/week, 5 times in total), or ATT-I + anti-PD-1 combo. Tumors were harvested 2 weeks after initial treatment (5 tumor samples were pooled per arm). (A) t-SNE plot of the scRNA-seq data collected from all conditions. Cell types were assessed by the expression levels of known marker genes. (B) Gene expression profiles of functional marker genes in selected immune cell types. Each row and column represents 1 gene and 1 cell type, respectively. (C) Averaged expression levels of T cell activation and cytotoxic marker genes in the CD8⁺ effector T cells from different conditions. The dot size characterizes the proportion of CD8⁺ effector T cells of each condition (y axis) with expression levels (indicated by color intensity) of the selected genes (x axis). The dot color reflects the averaged expression level of each gene in the CD8⁺ effector T cells of each condition. (D) Distribution of cytotoxicity scores of CD8⁺ effector T cells under each condition. Cytotoxic level of each cell is inferred by the averaged expression level of CD8⁺ T marker genes *Prf1*, *Ifng*, *Tnf*, *Pdcdf*, *Sla2*, and *Cd8a*. The y axis represents the cytotoxicity score. Combo versus anti-PD-1 ($P = 1.121 \times 10^{-6}$); combo versus ATT-I ($P = 0.0024$). Statistical analysis was conducted using unpaired 2-tailed t test. (E) Proportion of CD8⁺ effector T cells with significant cytotoxicity genes expressed. The y axis represents the proportion of CD8⁺ effector T cells with (dark blue) and without (red) significant cytotoxicity genes expressed. Combo versus anti-PD-1 ($P = 1.006 \times 10^{-9}$), combo versus ATT-I ($P = 3.816 \times 10^{-5}$), combo versus control ($P = 1.557 \times 10^{-8}$). Statistical analysis was conducted using Fisher's exact test.

drich) and 1% penicillin-streptomycin solution (10,000 U/mL penicillin + 10,000 µg/mL streptomycin, HyClone). CT26 cells were maintained in RPMI medium supplemented with 10% FBS and 1% penicillin-streptomycin solution. Cell lines were cultured at 37°C in a humidified incubator with 5% CO₂.

CD8⁺ T cell cytotoxicity assay. To generate mature CTLS, splenocytes were isolated from OT-I mice and stimulated with 5 µg/mL OVA₂₅₇₋₂₆₄ (S7951-1MG, MilliporeSigma) in the presence of 10 ng/mL IL-2 for 3 days. T cells were then centrifuged and cultured in RPMI 1640 medium containing 10 ng/mL murine IL-2, 10% FBS, and 1% penicillin-streptomycin. To measure the cytotoxicity of CD8⁺ T cells, 50,000 enriched CD8⁺ T cells were mixed in 96-well plates with MC38-OVA cells at ratios of 5:1, 1:1, or 1:5. ATT-I was added to MC38 cells or CD8⁺ T cells 48 hours before coculture. We assessed the kill-

ing efficiency by measuring the activity of luciferase (E1910, Dual-Luciferase Reporter Assay System, Promega) after 6 hours of coculture of the T cells together with the tumor cells.

Tumor implantation and treatment. For the orthotopic injection of MC38 colorectal cancer cells in the cecum, mice were anesthetized and shaved around the belly. To expose the cecum, we made a small incision of the skin and muscle. MC38 cells expressing luciferase were injected in a final volume of 50 µL PBS containing 2×10^5 cells using a 30 gauge needle. The cecum was repositioned in the mice and the wound was closed using surgical sutures and wound clips. For subcutaneous tumor experiments, 1×10^5 MC38 cells or 5×10^4 CT26 cells were injected in a final volume of 50 µL PBS using a 30 gauge needle. Mice were randomly allocated into the different groups 7 days after tumor implantation. Anti-PD-1 (clone RMP1-14; BioXCell) or isotype

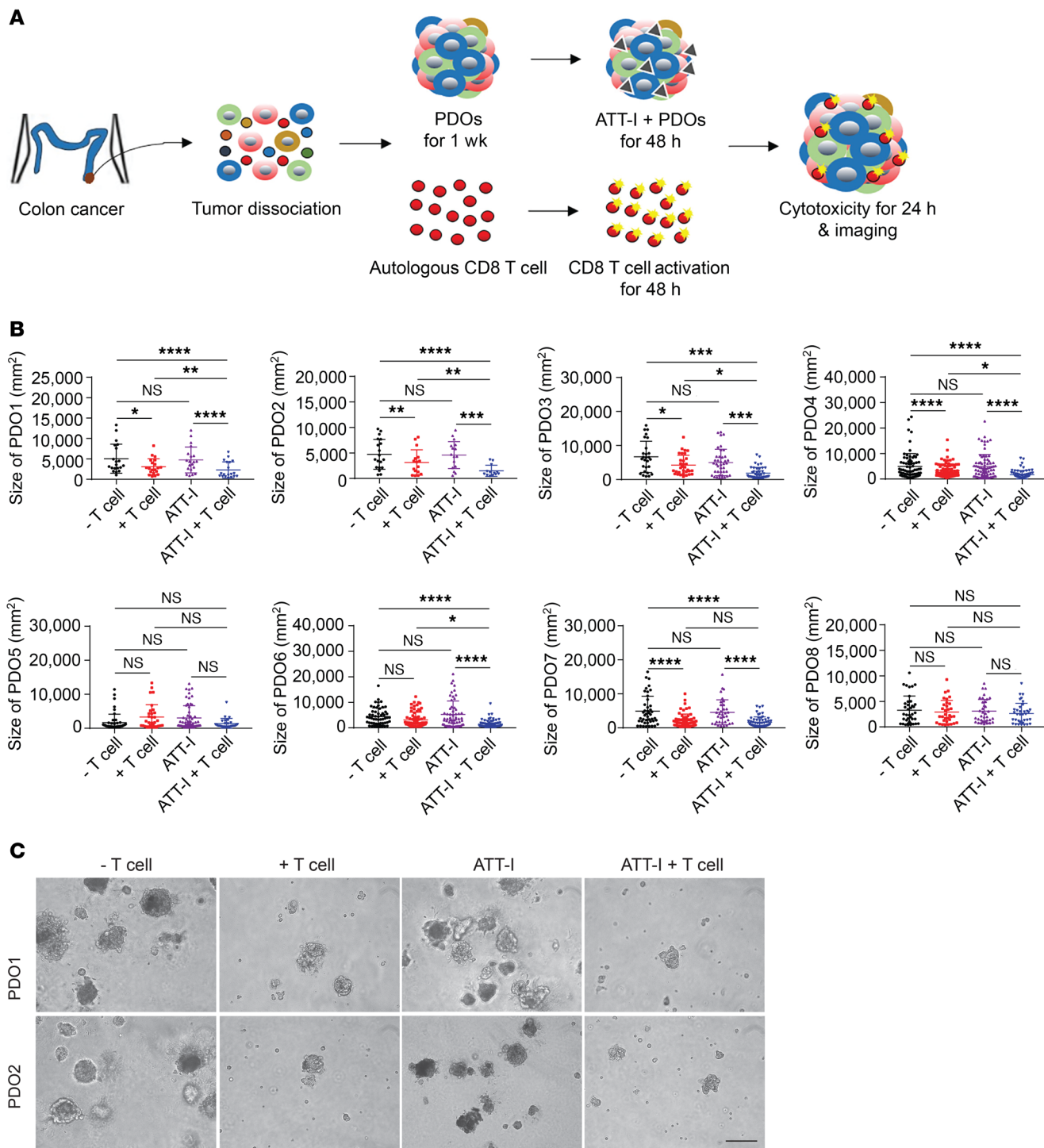


Figure 9. ATT-I enhances the autologous T cell responses in CRC patient-derived tumor organoids. (A) Schematic representation of patient-derived organoids (PDOs) cocultured with autologous CD8⁺ T cells in the presence or absence of ATT-I. **(B)** Quantification of the organoid size presented as mean \pm SD from 8 different patients (PDO1-PDO8). The size of organoids was measured as project area (μm^2) using Image J software. Statistical analysis was conducted using 1-way ANOVA. **(C)** Microscopic images of PDOs cocultured with autologous CD8⁺ T cells in the presence or absence of ATT-I (30 μM) from patient 1 (PDO1) and patient 2 (PDO2). Scale bar: 100 μm . * P < 0.05; ** P < 0.01; *** P < 0.001; **** P < 0.0001.

control (clone 2A3; BioXCell) treatment was administered intraperitoneally 3 times per week for a total of 5 injections at 200 $\mu\text{g}/\text{mouse}$. ATT-I was administered intraperitoneally every day at 50 mg/kg bodyweight. Our ATT-I treatment dose was selected based on previously reported publications using a range of 20 to 75 mg/kg (39, 40).

For the depletion experiment, anti-CD4 (clone GK1.5; BioXCell), anti-CD8 (clone 53-6.72; BioXCell), anti-CD20 (clone AISB12; BioXCell), and isotype (clone 2A3; BioXCell) antibodies were administered 3 times per week. The antibodies were administered 2 days prior to tumor cell inoculation and the injection continued until the end of the

experiment. Orthotopic tumor growth was monitored by *in vivo* bioluminescence tumor imaging using IVIS Spectrum after intraperitoneal injection of 200 μ L of 15 mg/mL luciferin (Potassium Luciferin; Gold Biotechnology). The fluorescence signal was acquired 15 minutes after the substrate administration.

CyTOF sample processing and data analysis. Tumors were excised and manually cut to 2 mm \times 2 mm pieces. They were then both enzymatically and mechanically dissociated according to the manufacturers' procedures using the mouse tumor dissociation kit and GentleMACS Dissociator (Miltenyi Biotec). The cells were further filtered using a 100 micron filter (BD Falcon). After centrifugation, the red blood cells were lysed (Biolegend), neutralized, washed, and resuspended in house-made CyTOF buffer (cold PBS containing 0.5% BSA and 0.02% Azide). For each sample 1.5×10^6 cells were used. CyTOF data were evaluated via viSNE analysis using the Cytobank platform (41). viSNE analysis allows the visualization of a high dimensional analysis in 2 dimensions using the Barnes-Hut implementation of the t-distributed stochastic neighbor embedding (tSNE) algorithm. We ran the viSNE analysis on the samples through a proportional sampling, with 7500 iterations, a perplexity of 30 and a theta of 0.5. On this viSNE analysis we performed SPADE clustering. The cell populations were then manually gated on the SPADE tree based on the selected markers. Hereafter, these clustered cell populations were visualized on viSNE as an overlaid plot.

Microscale thermophoresis analysis. Purified PSMD4 protein was labeled with Alexa Fluor 647 (Thermo Fisher Scientific, A20173). Compounds were titrated between 1 to 500,000 nM to a constant amount of Alexa Fluor 647-labeled PSMD4. The samples were incubated at room temperature for 10 minutes before the measurements. The binding assay was performed in a buffer with 20 mM Tris, 100 mM NaCl, and 0.02% Tween-20. A NanoTemper Monolith Instrument (NT.115) was used for measuring thermophoresis. Standard capillaries (catalog K002, NanoTemper) were used in the experiments. Thermophoresis of the protein in presence of compound was analyzed for 30 seconds. Measurements were performed at room temperature.

Immunoproteasome assay. Using the immunoproteasome activity fluorometric assay (UBPBio, catalog J4170), we determined the chymotrypsin-like, trypsin-like, and caspase-like activities of MC38-OVA, MC38-OVA-PSMD4^{loss}, and MC38-OVA-PSMD7^{loss} tumor cells treated with and without 30 μ M ATT-I treatment. After 48 hours of treatment, the cells were lysed with ice-cold cell lysis buffer to release the immunoproteasome. The protein concentrations were quantified by Pierce BCA Protein Assay kit (Thermo Fisher Scientific, catalog 23227). The respective immunoproteasome cleavage capacity on each of the substrates was determined using the AMC fluorescence detected at the 360 nm excitation and 460 nm emission wavelength. The incubation periods and substrates were used according to the manufacturer's guidelines.

Generation of murine and human patient-derived tumor organoids. MC38 OVA tumors and human colorectal cancer samples (obtained using an approved institutional protocol and patient consent) were cut to small pieces (3 mm \times 3 mm), processed into small pieces using the MACS Dissociator (Miltenyi Biotec) and digested to single cells using the mouse or human tumor isolation kit, respectively, according to manufacturer's guidelines (Miltenyi Biotec). The isolated cells were cultured overnight with F12/DMEM, 10% FBS culture medium, supplemented with 1% penicillin-streptomycin and 150 U/mL murine IL-2 (catalog 575402, Biolegend) or human IL-2 (catalog

589102, Biolegend). Adherent cells were harvested to generate organoids. For human clinical samples, the CD8⁺ T cells were also enriched by anti-human CD8⁺ T cell beads and stimulated by the human T activator CD3/ CD28 Dynabeads (Miltenyi Biotec). The CD8⁺ T cells were expanded in the F12/DMEM, 10% FBS culture medium supplemented with IL-2. The adherent cells were suspended with a concentration of 2×10^5 cells/mL in the human intestinal stem cell minus Wnt culture medium containing 10% Matrigel Basement Membrane Matrix (Corning, catalog 356255), which has been reported for generation of colorectal tumor organoids (42). The cells were seeded in a 6-well culture plate with ultra-low attachment surface (Corning) with a total volume of 2 mL per well. The cells were cultured for 1 week to generate organoids. Every 2 to 3 days culture medium was added with same volume and split in 2 wells. The murine organoids with diameter of 70 to 150 μ m were filtered sequentially by 70 μ m and then 150 μ m cell strainers (70 μ m, Thermo Fisher Scientific, catalog 07201431; 150 μ m, pluriStrainer, catalog 43-50150-03). The MC38 OVA organoids were treated with and without drug for 48 hours and then were cocultured with the CD3/ CD28 bead-activated CD8⁺ T cells isolated from OT-I mice for 24 hours. The patient-derived tumor organoids were cocultured with autologous CD8⁺ T cells. The organoids were imaged under optical microscope, digested into single cells, and analyzed by flow cytometry. The organoid size was analyzed using Image J software 1.50e.

Data availability. The scRNA-Seq data used in this study have been deposited in the NCBI Gene Expression Omnibus (GEO GSE171158).

Statistics. Statistical analysis was conducted using GraphPad Prism and R. Comparison of 2 data sets was done using 2-tailed unpaired student's *t* test. Comparison of more than 2 data sets was done using 1-way ANOVA followed by Bonferroni's multiple comparison test. For tumor growth assays, we used 2-way ANOVA followed by Tukey's multiple comparisons test. The results are displayed as the mean \pm SD or SEM. Kaplan-Meier plots are used for survival curves and analyzed using the log-rank test. The number of asterisks indicates the level of significance: **P* < 0.05; ***P* < 0.01; ****P* < 0.001, and *****P* < 0.0001. For the scRNA-seq, downstream analysis of those matrices was conducted by Seurat (v3.1). Cell filtering follows 2 criteria for all samples: (a) detected number of RNA in a single cell should be over 500, and (b) the percentage of mitochondria genes detected in a single cell should not exceed 15%. The remaining cells from each sample were merged and log-normalized. PhenoGraph in Seurat was applied to cluster cells with resolution set as 0.5. Low dimensional t-SNE visualization was computed by Rtsne package using normalized transcriptional expression profile with perplexity setting as 30. Each cell cluster is annotated by marker genes found by FindAllMarkers function in Seurat. Significant expression of cytotoxic marker genes in each CD8⁺ T cell were computed by using left truncated mixture Gaussian model. Statistical analysis for CETSA was described in detail and included in the Methods.

Study approval. All mice were housed in the Laboratory Animal Resource Center of Indiana University and all procedures were carried out in accordance with approval of the Institutional Animal Care and Use Committee animal protocols at Indiana University.

Author contributions

KVDJ, CH, GJ, and XL conceived, coordinated, and designed the study. HX, KVDJ, ZZ, LZ, Y Li, TY, DL, MF, YF, XH, XZ, Y Liu, and ABW performed experiments. KVDJ, CW, YS, KMS, CZ, and XL

analyzed the bioinformatics data. ZZ generated the organoids and analyzed the organoid killing data. HX and KVDJ analyzed the microscopy data. CH and GJ provided the compound library. ABW and ALM performed and analyzed the CETSA assay. GES assessed the pathological score on histology samples. SOM performed the structure analysis and ligand-interaction diagram. HX, KVDJ, ZZ, and XL interpreted the results. KVDJ and XL wrote the manuscript with input from all authors.

Acknowledgments

We thank Małgorzata Maria Kamocka for her technical assistance. The authors thank the members of the Indiana University Melvin and Bren Simon Cancer Center Flow Cytometry Resource Facility (FCRF) for their technical support. We thank the IU Simon Com-

prehensive Cancer Center for the use of the Tissue Procurement & Distribution Core, which provided fresh CRC tumor samples to this study. We also thank the Angio BioCore for the use of the IncuCyte. The study is supported in part by the Indiana University School of Medicine (IUSM) Strategic Research Initiative fund (to XL). KVDJ is the Walter A. and Laura W. Deutsch Scholar.

Address correspondence to: Cheng Huang, 1200 Cailun Road, Shanghai 201203, China. Phone: 8621.5132.3194; Email: chuang@shutcm.edu.cn. Or to: Ji Guang, 725 Wanping South Road, Shanghai 200032, China. Phone: 8621.6438.5700, ext. 9501; Email: jiliver@vip.sina.com. Or to: Xiongbin Lu, 980 W. Walnut Street, R3.C218D, Indianapolis, Indiana 46202, USA. Phone: 317.274.4398; Email: xiolu@iu.edu.

1. Wallich R, et al. Abrogation of metastatic properties of tumour cells by de novo expression of H-2K antigens following H-2 gene transfection. *Nature*. 1985;315(6017):301–305.
2. Sade-Feldman M, et al. Resistance to checkpoint blockade therapy through inactivation of antigen presentation. *Nat Commun*. 2017;8(1):1136.
3. Hulpke S, Tampe R. The MHC I loading complex: a multitasking machinery in adaptive immunity. *Trends Biochem Sci*. 2013;38(8):412–420.
4. Spranger S, Gajewski TF. Impact of oncogenic pathways on evasion of antitumour immune responses. *Nat Rev Cancer*. 2018;18(3):139–147.
5. Beatty GL, Gladney WL. Immune escape mechanisms as a guide for cancer immunotherapy. *Clin Cancer Res*. 2015;21(4):687–692.
6. Leone P, et al. MHC class I antigen processing and presenting machinery: organization, function, and defects in tumor cells. *J Natl Cancer Inst*. 2013;105(16):1172–1187.
7. Fang Y, et al. MAL2 drives immune evasion in breast cancer by suppressing tumor antigen presentation. *J Clin Invest*. 2021;131(1):e140837.
8. Bukur J, et al. The role of classical and non-classical HLA class I antigens in human tumors. *Semin Cancer Biol*. 2012;22(4):350–358.
9. Donia M, et al. Acquired immune resistance follows complete tumor regression without loss of target antigens or IFN γ signaling. *Cancer Res*. 2017;77(17):4562–4566.
10. Ribas A, Wolchok JD. Cancer immunotherapy using checkpoint blockade. *Science*. 2018;359(6382):1350–1355.
11. Couzin-Frankel J. Breakthrough of the year 2013. Cancer immunotherapy. *Science*. 2013;342(6165):1432–1433.
12. Van der Jeught K, et al. Targeting the tumor microenvironment to enhance antitumor immune responses. *Oncotarget*. 2015;6(3):1359–1381.
13. Van der Jeught K, et al. Drug resistance and new therapies in colorectal cancer. *World J Gastroenterol*. 2018;24(34):3834–3848.
14. Van der Jeught K, et al. ST2 as checkpoint target for colorectal cancer immunotherapy. *JCI Insight*. 2020;5(9):e136073.
15. de Charette M, et al. Turning tumour cells into antigen presenting cells: The next step to improve cancer immunotherapy? *Eur J Cancer*. 2016;68:134–147.
16. Galluzzi L, et al. Immunogenic cell death in cancer and infectious disease. *Nat Rev Immunol*. 2017;17(2):97–111.
17. Odendaal AY, et al. Chemoselective enrichment for natural products discovery. *Chem Sci*. 2011;2(4):760–764.
18. More S, Choi DK. Neuroprotective role of atractylenolide-I in an *in vitro* and *in vivo* model of parkinson's disease. *Nutrients*. 2017;9(5):E451.
19. Wang CC, et al. Pro-oxidant and cytotoxic activities of atractylenolide I in human promyeloleukemic HL-60 cells. *Food Chem Toxicol*. 2006;44(8):1308–1315.
20. Martinez Molina D, et al. Monitoring drug target engagement in cells and tissues using the cellular thermal shift assay. *Science*. 2013;341(6141):84–87.
21. Lander GC, et al. Complete subunit architecture of the proteasome regulatory particle. *Nature*. 2012;482(7384):186–191.
22. Lasker K, et al. Molecular architecture of the 26S proteasome holocomplex determined by an integrative approach. *Proc Natl Acad Sci USA*. 2012;109(5):1380–1387.
23. Stone HR, Morris JR. DNA damage emergency: cellular garbage disposal to the rescue? *Oncogene*. 2014;33(7):805–813.
24. Riedinger C, et al. Structure of Rpn10 and its interactions with polyubiquitin chains and the proteasome subunit Rpn12. *J Biol Chem*. 2010;285(44):33992–34003.
25. McCarthy MK, Weinberg JB. The immunoproteasome and viral infection: a complex regulator of inflammation. *Front Microbiol*. 2015;6:21.
26. Efremova M, et al. Targeting immune checkpoints potentiates immunoediting and changes the dynamics of tumor evolution. *Nat Commun*. 2018;9(1):32.
27. Li L, et al. Potential reproductive toxicity of Large-head Atractylodes Rhizome, the most commonly used Chinese medicine for threatened miscarriage. *Hum Reprod*. 2011;26(12):3280–3288.
28. Mita Y, et al. Crucial role of CD69 in anti-tumor immunity through regulating the exhaustion of tumor-infiltrating T cells. *Int Immunol*. 2018;30(12):559–567.
29. Fujiyoshi K, et al. Metastatic pattern of stage IV colorectal cancer with high-frequency microsatellite instability as a prognostic factor. *Anticancer Res*. 2017;37(1):239–247.
30. Popat S, et al. Systematic review of microsatellite instability and colorectal cancer prognosis. *J Clin Oncol*. 2005;23(3):609–618.
31. Kim TK, et al. Defining and understanding adaptive resistance in cancer immunotherapy. *Trends Immunol*. 2018;39(8):624–631.
32. Winter MB, et al. Immunoproteasome functions explained by divergence in cleavage specificity and regulation. *Elife*. 2017;6:e27364.
33. Angeles A, et al. Immune and non-immune functions of the immunoproteasome. *Front Biosci (Landmark Ed)*. 2012;17:1904–1916.
34. Kalaora S, et al. Immunoproteasome expression is associated with better prognosis and response to checkpoint therapies in melanoma. *Nat Commun*. 2020;11(1):896.
35. Styers ML, et al. Depletion of beta-COP reveals a role for COP-I in compartmentalization of secretory compartments and in biosynthetic transport of caveolin-1. *Am J Physiol Cell Physiol*. 2008;294(6):C1485–C1498.
36. Chen X, et al. Quantitative proteomics analysis of cell cycle-regulated Golgi disassembly and reassembly. *J Biol Chem*. 2010;285(10):7197–7207.
37. Razi M, et al. Early endosomes and endosomal coatamer are required for autophagy. *J Cell Biol*. 2009;185(2):305–321.
38. Malemo I, et al. Frequent loss of heterozygosity in the $\beta 2$ -microglobulin region of chromosome 15 in primary human tumors. *Immunogenetics*. 2011;63(2):65–71.
39. Xiao Q, et al. Repression of PDK1- and LncRNA HOTAIR-mediated EZH2 gene expression contributes to the enhancement of atractylenolide 1 and Erlotinib in the inhibition of human lung cancer cells. *Cell Physiol Biochem*. 2018;49(4):1615–1632.
40. Zhang WL, et al. Establishment of a mouse model of cancer cachexia with spleen deficiency syndrome and the effects of atractylenolide I. *Acta Pharmacol Sin*. 2020;41(2):237–248.
41. Amir EaD, et al. viSNE enables visualization of high dimensional single-cell data and reveals phenotypic heterogeneity of leukemia. *Nat Biotechnol*. 2013;31(6):545–552.
42. van de Wetering M, et al. Prospective derivation of a living organoid biobank of colorectal cancer patients. *Cell*. 2015;161(4):933–945.